Double-slit interference effect in electron emission from H_2^+ exposed to x-ray radiation

Xiaoxu Guan,[1] Ethan B. Secor,[1] Klaus Bartschat,[1] and Barry I. Schneider[2]
[1]*Department of Physics and Astronomy, Drake University, Des Moines, Iowa 50311, USA*
[2]*Office of Cyberinfrastructure, National Science Foundation, Arlington, Virgina 22230, USA*
(Received 2 March 2012; published 23 April 2012)

We consider the photoionization of the hydrogen molecular ion exposed to x-ray radiation for photon energies up to 500 eV in the fixed-nuclei approximation. The temporal development of the system is described by a fully *ab initio* time-dependent grid-based approach in prolate spheroidal coordinates. At sufficently high photon energies, the angular distributions of the electron ejected from the two-center diatomic target resemble the classical double-slit-like interference pattern more closely when the molecular axis and the linear laser polarization direction are perpendicular to each other than in the parallel geometry. Both the preferable emission modes and the confinement effect (in the parallel geometry) of the photoelectron also map out in the time evolution of the wave packets. The validity of a simple plane-wave model is analyzed by comparing its predictions with those from our accurate *ab initio* calculations.

DOI: 10.1103/PhysRevA.85.043419 PACS number(s): 33.80.Wz, 31.15.A−

I. INTRODUCTION

The double-slit interference of photoelectrons emitted from diatomic molecules in the photon-energy regime of a few hundred eV was suggested by Cohen and Fano in 1966 [1] based on the presence of oscillations in the total cross sections for N_2 and O_2 targets as a function of photon energy. Rather than looking at angle-integrated cross sections, Kaplan and Markin [2] suggested that the two-center diffraction effect may be more likely visible in the angular distributions of the photoelectron. The classical interference pattern observed in these quantum molecular systems clearly demonstrated the wave nature of the electron emitted from the two separated nuclei [3,4].

Recent rapid experimental progress in intense laser sources as well as new imaging technology [5] has made it possible to investigate a comprehensive scenario of atomic and molecular targets interacting with ultrashort laser pulses or synchrotron light radiation. Cold-target recoil-ion momentum spectroscopy (COLTRIMS) experiments [6] deliver rich and complete momentum information through coincidence studies involving all charged fragments, i.e., electrons and nuclei, in the laser-atom or laser-molecule interaction. These ongoing experimental advances, together with the availability of sophisticated theoretical approaches, have sparked a broad interest in exploring multicenter diffraction patterns in the laser-molecule interaction.

Recent measurements [7,8] revealed a four-lobe structure in the angular distributions of the double ionization in H_2 after single-photon absorption of circularly polarized radiation with energies of 160 and 240 eV. The experimentalists attributed the four-lobe pattern in the angular distributions to the interference effect in the smallest microscopic double-slit device. Although theorists [9] offered an entirely different explanation for the structure, these experiments show the potential for detecting a two-center interference effect in diatomic molecules in the future. Indeed, nearly half a century after the original predictions of Cohen and Fano, oscillations in the angle-integrated cross sections of electron emission from diatomic molecules were experimentally observed in 2011 [10], using the third-generation synchrotron source at Lawrence Berkeley National Laboratory [11].

The neutral H_2 molecule is a strongly correlated system. Consequently, the double-slit phenomenon in nonsequential double photoionization, in which the two electrons are removed at the same time, is much more complicated than the effect would be in one-electron targets. In the present work, therefore, we first look at the simplest case: single-photon ionization of H_2^+ in the high-energy photon regime.

On the theoretical side, the problem has been addressed using both time-dependent and time-independent methods, with and without inclusion of the nuclear motion. Two-center effects in the diatomic molecules H_2^+, H_2, and Li_2^+ exposed to circularly polarized light were studied by Rescigno and collaborators [12,13]. Meanwhile, Yuan *et al.* [14,15] considered the laser-induced electron diffraction of H_2^+ and H_2 in a planar model of reduced dimensionality. An *ab initio* four-dimensional numerical simulation was performed by Hu *et al.* [16], who solved the time-dependent Schrödinger equation (TDSE) in Cartesian coordinates.

In the present work, we apply our recently developed time-dependent finite-element discrete-variable representation (FE-DVR), a grid-based approach [17] in prolate spheroidal coordinates, to study the double-slit interference effect of an H_2^+ molecular ion irradiated by intense linearly polarized x-ray laser pulses. The H_2^+ ion is treated in the fixed-nuclei approximation (FNA). The energy of the laser pulses ranges from 200 to 500 eV. This relatively simple test case has also been solved in one-center spherical coordinates [18,19] and Cartesian coordinates [16]. Prolate spheroidal coordinates, however, capture the essential multicenter characteristics for a simple diatomic molecule such as H_2^+, and they are also suitable to treat heavier diatomics, for which the spherical and Cartesian coordinate systems have serious disadvantages. Combined with an effective discretization scheme, benchmark results for the potential energy curves as well as the two-center Coulomb phase shifts of electronic continuum states can be readily obtained with very high accuracy. These results then allow us to judge the validity of the approximations made in simpler treatments.

For the double-slit phenomenon to be observable in diatomic targets, the de Broglie wavelength (λ_e) of the photoelectron must be smaller than the internuclear separation (R). At relatively low photon energy, this would require a large nuclear separation. For the equilibrium distance of $R_{\rm eq} = 2.0$ bohr in $H_2{}^+$, classical diffraction can be expected only at photon energies above 164 eV.

The present work is a proof-of-principle calculation using the FNA. This allows us to vary both the internuclear separation and the photon energy to detect potential interference behavior. Specifically, we scan the internuclear distance from 1 to 5 bohr and the photon energy from 200 to 500 eV. The latter photon energies are indeed experimentally available from modern synchrotron radiation facilities.

The remainder of the paper is organized as follows. After sketching our *ab initio* time-dependent formalism in Sec. II, we present results for angle-resolved differential cross sections in Sec. III and for probability densities of the electronic wave packets for single-photon ionization in Sec. IV. The paper concludes with a summary and an outlook in Sec. V.

II. THEORETICAL APPROACH

We use prolate spheroidal coordinates with the two foci located on the two nuclei with fixed internuclear separation R. In addition to the azimuthal angle φ ($0 \leqslant \varphi \leqslant 2\pi$), the "radial" ($1 \leqslant \xi < \infty$) and "angular" ($-1 \leqslant \eta \leqslant +1$) coordinates are defined as $\xi = (r_1 + r_2)/R$ and $\eta = (r_1 - r_2)/R$, respectively. Here r_1 and r_2 denote the distances measured from the electron to the two nuclei. We discretize the (ξ,η) coordinates as follows:

(1) The truncated ξ space ($\xi \leqslant \xi_{\rm max}$) is subdivided into a number of finite elements, and DVR bases are employed within each individual element. A Gauss-Radau quadrature (in the first element) or a Gauss-Lobatto quadrature (in the others) is employed to ensure continuity at the element boundaries.

(2) A single element with a set of Gauss quadrature points is used in the region $[-1,+1]$ for the η coordinate. If desired, multiple elements are also possible.

We refer the reader to [17,20] for more comprehensive discussions regarding the practical implementation of the FE-DVR approach in prolate spheroidal coordinates. Detailed information about our implementation of the Lanczos algorithm for the time propagation of the system can be found in Refs. [20,21] and will not be repeated here.

The physical information about the ionization process can be extracted by projecting the temporal wave packet at the end of the time evolution onto the relevant continuum states. We use the exact *ab initio* solution of the two-center Coulomb wave to extract the angular distributions. In prolate spheroidal coordinates, the partial-wave expansion of the continuum state $\Phi_{\boldsymbol{k}}^{(-)}(\boldsymbol{r})$ with momentum vector $\boldsymbol{k}$, satisfying the appropriate incoming boundary conditions, is written as

$$\Phi_{\boldsymbol{k}}^{(-)}(\boldsymbol{r}) = \frac{1}{k}\sum_{\ell m} i^{\ell} e^{-i\Delta_{|m|\ell}(k)} \mathcal{Y}^{*}_{\ell m}(\boldsymbol{k}) \mathcal{Y}_{\ell m}(k,\eta,\varphi) \Pi^{(k)}_{\ell m}(\xi), \quad (1)$$

where $\mathcal{Y}_{\ell m}$ and $\Pi^{(k)}_{\ell m}(\xi)$ are the angular "spheroidal harmonics" and radial functions, respectively, and $\Delta_{|m|\ell}(k)$ is the two-center Coulomb phase shift. The latter can be determined by normalizing the numerical solution to the known asymptotic behavior of the radial function,

$$\Pi^{(k)}_{\ell m}(\xi) \to \frac{1}{\xi R}\sqrt{\frac{8}{\pi}} \sin\left(\frac{kR}{2}\xi + \frac{2}{k}\ln(kR\xi) - \frac{\ell\pi}{2} + \Delta_{|m|\ell}(k)\right) \quad (2)$$

as $\xi \to +\infty$. This normalizes $\Phi_{\boldsymbol{k}}^{(-)}(\boldsymbol{r})$ to a δ function in momentum space, i.e., $\langle \Phi_{\boldsymbol{k}}^{(-)} | \Phi_{\boldsymbol{k}'}^{(-)} \rangle = \delta(\boldsymbol{k} - \boldsymbol{k}')$. The normalization of the continuum-state wave functions and the two-center Coulomb phase shift are obtained through matching the numerical solution of $\Pi^{(k)}_{\ell m}(\xi)$ to its asymptotic behavior in Eq. (2).

Projection of the time-dependent wave function at the end of the time evolution ($t = t_e$) onto the functions in Eq. (1) yields

$$\langle \Phi_{\boldsymbol{k}}^{(-)} | \Psi(t_e) \rangle = \frac{1}{k}\sum_{\ell m} (-i)^{\ell} e^{i\Delta_{|m|\ell}(k)} \mathcal{Y}_{\ell m}(\boldsymbol{k}) \mathcal{F}_{\ell m}(k), \quad (3)$$

where the partial-wave complex amplitude $\mathcal{F}_{\ell m}(k)$ in the (ℓ,m) ionization channel is given by

$$\mathcal{F}_{\ell m}(k) = \sum_{ij} \left(\frac{R}{2}\right)^{3/2} \sqrt{\xi_i^2 - \eta_j^2}\, \Pi^{(k)}_{\ell m}(\xi_i)\, \Xi^{(k)}_{\ell m}(\eta_j) C^{m}_{ij}(t_e). \quad (4)$$

Here $\Pi^{(k)}_{\ell m}(\xi_i)$ and $\Xi^{(k)}_{\ell m}(\eta_j)$ are the expansion coefficients of the radial and angular functions in terms of the normalized DVR $\{f_i(\xi)\}$ and $\{g_j(\eta)\}$ bases, respectively, while $C^{m}_{ij}(t_e)$ denotes the expansion coefficient of the wave function at $t = t_e$. This simple expression is a direct consequence of the FE-DVR representation.

The probability density for ionization within the momentum-space volume $d\boldsymbol{k}$ is given by

$$\frac{dP_{\rm ion}}{d\boldsymbol{k}} = |\langle \Phi_{\boldsymbol{k}}^{(-)} | \Psi(t_e) \rangle|^2. \quad (5)$$

Consequently, the probability density for ionization ($dP_{\rm ion}/d\Omega$) of the photoelectron scattered into the solid angle $d\Omega$ is

$$\frac{dP_{\rm ion}}{d\Omega} = \int k^2 dk |\langle \Phi_{\boldsymbol{k}}^{(-)} | \Psi(t_e) \rangle|^2 = \int dk \left| \sum_{\ell m} (-i)^{\ell} e^{i\Delta_{m\ell}(k)} \mathcal{Y}_{\ell m}(\boldsymbol{k}) \mathcal{F}_{\ell m}(k) \right|^2. \quad (6)$$

The quantity $dP_{\rm ion}/d\Omega$ will also be referred to as the angular distribution below.

When the concept of a cross section is appropriate [17], the above probability density for ionization can be converted to the differential cross section (DCS) through

$$\frac{d\sigma}{d\Omega} = \frac{\omega_0}{I_0}\frac{1}{T_{\rm eff}}\frac{dP_{\rm ion}}{d\Omega}. \quad (7)$$

Here ω_0 and I_0 are the central laser frequency and the peak intensity of the laser field, respectively, while $T_{\rm eff}$ denotes the effective interaction time for single-photon ionization.

Equation (6) shows that the two-center effect already manifests itself in the angular distribution through the coherent summation over the contributions from several ionization channels (ℓ,m), even for single-photon ionization. For the single-photon process, only ionization channels with parity $(-1)^{\ell} = -1$ can contribute. This result is independent of the relative orientation between the molecular axis and the laser polarization direction. Unlike its atomic counterpart, the nonspherical potential in molecules may lead to amplitudes from other than the p channel ($\ell = 1$) dominating the angular distributions. In fact, contributions from the f channel ($\ell = 3$) or even higher ℓ channels can overwhelm those from the p channel. Therefore, angular distributions of electrons emitted from a diatomic molecule may exhibit characteristics that deviate from the well-known dipole pattern observed in atoms.

III. RESULTS AND DISCUSSION

The calculations described below were carried out for linearly polarized laser pulses with a peak intensity of 10^{16} W/cm^2. Since even the lowest photon energy is several hundred eV, the intensity still falls into the perturbative regime. Here we are interested only in ultrashort x-ray pulses with duration of 160–410 as. The ξ box can therefore safely be truncated at $\xi_{\max} = 400$. Tests showed that the results for the angular distributions extracted from a box with $\xi_{\max} = 500$ did not change within the line thickness shown in the figures below. The essential difference compared to our previous work [17] lies in the higher photon energies considered here. The ionized electronic wave packet contains much higher momentum components, e.g., $k \simeq 5.2$ atomic units (a.u.) when the ionization occurs at $R = 3.2$ bohr at a photon energy of 400 eV. Thus, even in the asymptotic region, the mesh points need to be rather dense in order to resolve the rapid oscillations of the wave packet. We used up to 2200 mesh points in the ξ box to ensure enough points to span the de Broglie wavelength ($\lambda_e = 2\pi/k$) of the photoelectron and hence to guarantee well-converged angular distributions in both shape and magnitude. The physical information was extracted using the procedure outlined in the previous section, after solving the TDSE with our parallelized Arnoldi-Lanczos method.

Classically, the bright and dark fringes in the double-slit interference pattern correspond to $R \sin\theta_n = n\lambda_e$ and $R \sin\theta_n = (n + 1/2)\lambda_e$, respectively, where n is an integer. Note that the emission angle θ_n is measured with respect to the direction *perpendicular* to the molecular axis, i.e., the line connecting the two "slits." Hence, the relationship $\lambda_e \lesssim R$ needs to be satisfied in order to observe the interference pattern. Below we discuss the similarities and differences between the angular distribution of photoelectrons from a quantal two-center molecule and classical two-slit-like interference. We will show that there are subtle differences between the quantum DCS and the classical double-slit experiment. Note that Baltenkov *et al.* [22] also argue that the resemblance between the diffraction effect predicted by Cohen and Fano [1] and that from the double-slit device has been vastly exaggerated, even though the two arrangements share some common features.

A. Angular distributions in the parallel geometry

Figures 1 and 2 display the angular distributions of the photoelectron emitted from the H_2^+ molecular ion in the "parallel" geometry, where the electric field of the linearly polarized radiation is parallel to the internuclear axis, for photon energies of 200, 300, 400, and 500 eV. At the smallest internuclear separation of 1.0 bohr considered here, the criterion ($\lambda_e \lesssim R$) is not satisfied for all the above photon energies. As expected, therefore, we only observe a dipolelike two-lobe structure, indicating that the electron prefers to be emitted along the laser polarization axis. Increasing the internuclear separation yields a larger momentum of the ionized electron, and thus a smaller de Broglie wavelength, so that the interference criterion can be met. Consider, for example, the case of 300 eV photon energy. The interference criterion is met if $R \gtrsim 1.42$ bohr. When the internuclear separation is increased further, the two-lobe structure gets wider and wider, finally evolving into a four-lobe structure. At the same time, the dipolelike emission mode is strongly suppressed. At the equilibrium distance $R_{\rm eq} = 2.0$ bohr, the photoelectron emission mode along the polarization direction

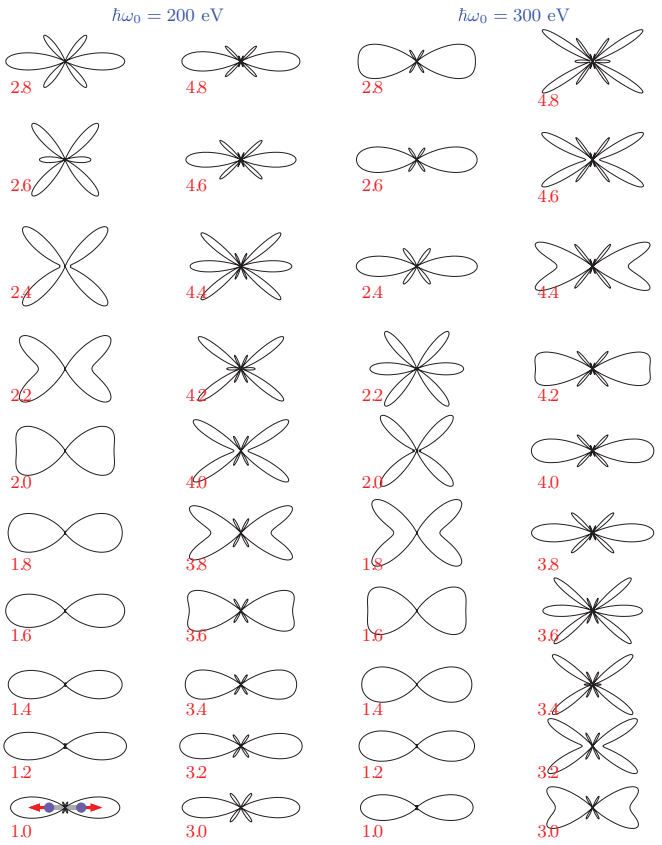

FIG. 1. (Color online) Angular distributions of the photoelectron emitted from the H_2^+ ion. The molecular axis is oriented along the direction of the laser polarization (see bottom left panel for illustration). The two left columns correspond to angular distributions at the photon energy of 200 eV, while the two right columns are for 300 eV. The angular distributions were scaled to the same magnitude. The label in each panel denotes the internuclear separation distance R, which ranges from 1.0 to 4.8 bohr.

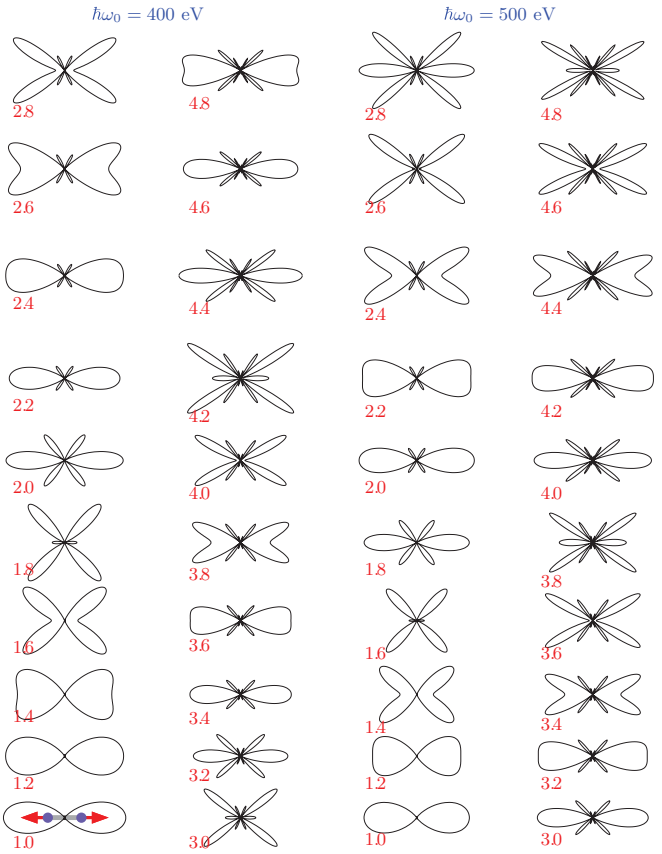

FIG. 2. (Color online) Same as Fig. 1, but for photon energies of 400 eV (the two left columns) and 500 eV (the two right columns).

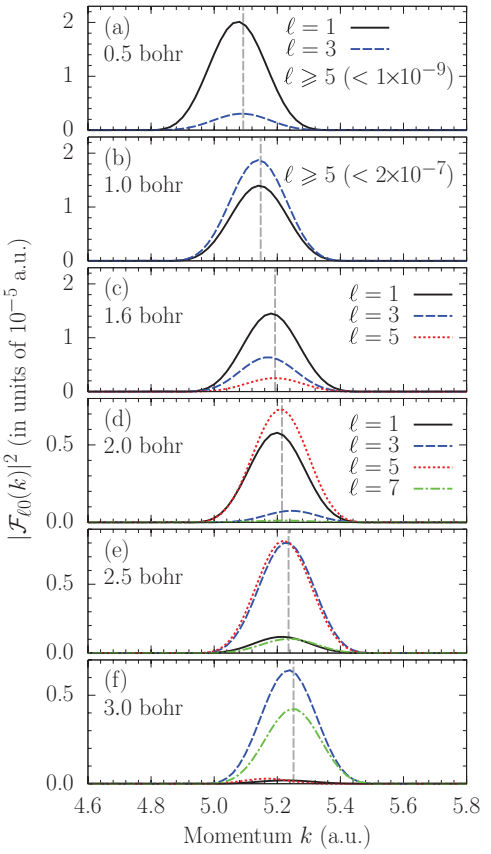

FIG. 3. (Color online) The function $|\mathcal{F}_{\ell 0}(k)|^2$ at the photon energy of 400 eV extracted from the time-dependent calculations with a peak intensity of 10^{16} W/cm^2 in a 20-cycle pulse with a sine-squared envelope function. The internuclear distance R takes values of (a) 0.5, (b) 1.0, (c) 1.6, (d) 2.0, (e) 2.5, and (f) 3.0 bohr. The vertical dashed line in each panel indicates the classical momentum $\sqrt{2[\hbar\omega_0 - I_0(R)]}$, where $I_0(R)$ is the ionization threshold at R.

has indeed disappeared completely at the photon energy of 300 eV.

This phenomenon depends sensitively on the combination of R and k. We therefore refer to it as the *dynamically* forbidden mode, in contrast to being *geometrically* forbidden by a selection rule. From Figs. 1 and 2, we also observe that the disappearance of the dipolelike emission is always accompanied by the emergence of new lobes. These additional lobes (at $\theta_1, \theta_2, \ldots$) in the angular distributions correspond to the first-order and second-order bright fringes in the classical optical double-slit interference. At $\hbar\omega_0 = 500$ eV and $R = 3.6$ bohr, for example, $\theta_1 \simeq 18.2^\circ$, $\theta_2 \simeq 36.7^\circ$, and $\theta_3 \simeq 61.2^\circ$ (again, with respect to the normal direction to the molecular axis) are obtained by solving the TDSE, while the values are 17.1°, 36.1°, and 62.1°, respectively, in the double-slit scenario.

We clearly see that the positions of the maxima in the angular distributions and the bright fringes in the classical double-slit device are in excellent agreement. However, this is not the case for the intensities of the maxima when we compare the double-slit interference pattern with the quantal DCSs of the photoelectron from the H_2^+ target. The classical intensities of the bright fringes fade with increasing angle θ_n. In the H_2^+ ion, on the other hand, the magnitude of the DCS at θ_2 is significantly larger than at θ_1 (cf. Fig. 2). In the classical double-slit interference pattern, the brightest fringe always appears at $\theta_0 = 0^\circ$. In the parallel geometry, however, the emission of the photoelectron along this direction (i.e., perpendicular to the internuclear axis) is geometrically forbidden.

In order to shed more light on this nonclassical behavior, we now present a partial-wave analysis based on the contributions from various ionization channels. Figure 3 shows the squared magnitudes of the complex ionization amplitude, $|\mathcal{F}_{\ell m}(k)|^2$, for selected R values at the photon energy of 400 eV [cf. Eq. (4)]. At a small internuclear separation, e.g., $R = 0.5$ bohr, the p channel indeed dominates the back-to-back two-lobe emission mode in the angular distribution. At this high photon energy, however, even the two-lobe structure at $R \simeq 1.0$ bohr observed in Fig. 2 is actually due to a strong mixture of contributions from the p and f channels, rather than a representation of pure p-channel characteristics. When R increases to 2.5 bohr, the influence of the p channel fades quickly, and the contributions from channels with higher ℓ dominate. This illustrates that the back-to-back mode observed in most cases may be due to entirely different angular symmetries, although they appear similar in shape.

The two-center nonspherical potential causes an increased influence of the higher angular momenta in the initial-state wave function when the molecular size deviates significantly from the united-atom ($R = 0$) limit. Consequently, it shows

the characteristics of the higher ℓ values in the angular distributions through the dipole coupling of $\ell \pm 1$ with the initial state. At this point, it is understandable that multilobe patterns in the angular distributions at large R and large photon energy originate from higher-order spherical harmonics. The high angular momenta in the initial state are therefore reflected in the angular distributions of the photoelectron. Our conclusion coincides with the findings of Baltenkov *et al.* [22], who arrived at them from an analysis of a zero-range model potential.

Figures 1 and 2 also exhibit the pattern of dynamically forbidden emission along the polarization axis at some particular combinations of $\hbar\omega_0$ and R. According to the simple plane-wave model of Walter and Briggs [23], the angular distribution is proportional to $(\boldsymbol{\epsilon}\cdot\boldsymbol{k})^2\cos^2(\boldsymbol{k}\cdot\boldsymbol{R}/2)$. In the parallel geometry, therefore, emission along the $\boldsymbol{\epsilon}$ direction is dynamically forbidden only if the condition $kR = n\pi$, where n is an odd integer, is satisfied. The phenomenon of strongly suppressed emission along the polarization direction was termed the "confinement effect" by Fernández *et al.* [12,13], since it resembled the situation of a quantum particle confined to an infinitely deep well.

Note that the confinement effect occurs only in the parallel geometry, but not in the perpendicular geometry (see below). Close examination shows that in most cases the above criterion for the confinement effect approximately coincides with our accurate numerical predictions. At the photon energy of 200 eV, for example, confinement happens at $R = 2.4$ bohr and $k = 3.56$ a.u. (cf. Fig. 1), and therefore $kR = 2.7\pi \approx 3\pi$. The plane-wave model also predicts that the confinement effect appears periodically, sensitively depending on both the photon energy and R. These predictions are in qualitative agreement with our accurate numerical results.

In Fig. 4 we further examine the validity of the plane-wave model in the prediction of the confinement effect. For the higher photon energy, we generally notice that the plane-wave model slightly overestimates the internuclear separation where the effect occurs. For example, our numerical result shows that confinement occurs at $R \simeq 4.63$ bohr, while the plane-wave model predicts it at $R \simeq 4.75$ bohr. This corresponds to $n = 9$. For near-threshold ionization (i.e., low photon energy such as $\hbar\omega_0 = 50$ eV), the plane-wave model predicts a forbidden emission mode along the $\boldsymbol{\epsilon}$ axis to manifest itself at $R \approx 6.2$ bohr. Our *ab initio* calculation, however, shows no confinement in this region of R for this low photon energy. For near-threshold ionization, we observe that the chance for the electron to be ejected along the $\boldsymbol{\epsilon}$ direction may be small in some cases, but it is not negligible compared to the dominant peaks. In other words, the plane-wave model is not accurate for near-threshold ionization, but it seems to catch the dominant features if the photon energy is as high as a few hundred eV.

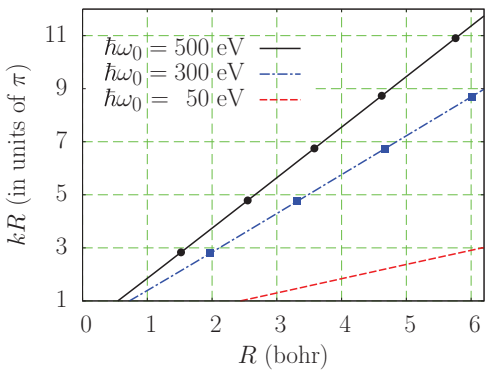

FIG. 4. (Color online) The function kR plotted against the internuclear distance R in the parallel geometry. The photon energies are 50, 300, and 500 eV, respectively. The circles (●) and squares (■) denote where the confinement effects are predicted in our *ab initio* time-dependent calculations.

B. Angular distributions in the perpendicular geometry

Figures 5 and 6 display the angular distributions in the "perpendicular" geometry, where the electric field of the linearly polarized radiation is perpendicular to the internuclear axis, for the same photon energies and R values as in Figs. 1 and 2. In this geometry, the confinement effect along the polarization direction completely vanishes. Instead of being forbidden, ejection along the polarization axis is a favorite escape mode for the photoelectron in the perpendicular geometry.

This feature can also be explained qualitatively with the plane-wave model. In the perpendicular geometry, electron emission along the molecular axis is forbidden. Equation (1) shows that there is a node in the continuum-state wave function $\Phi_{\boldsymbol{k}}^{(-)}(\boldsymbol{r})$ with Π symmetry, if $\boldsymbol{k}$ is oriented along the molecular

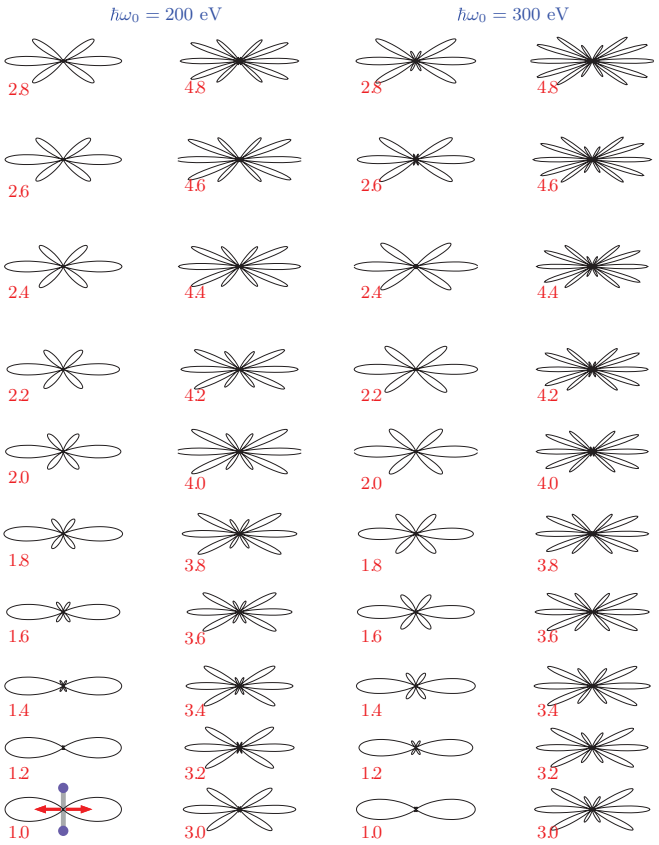

FIG. 5. (Color online) Same as Fig. 1, but for the perpendicular geometry. The molecular axis and the polarization direction (double-headed arrow in the bottom left panel) are oriented along the vertical and horizontal directions, respectively.

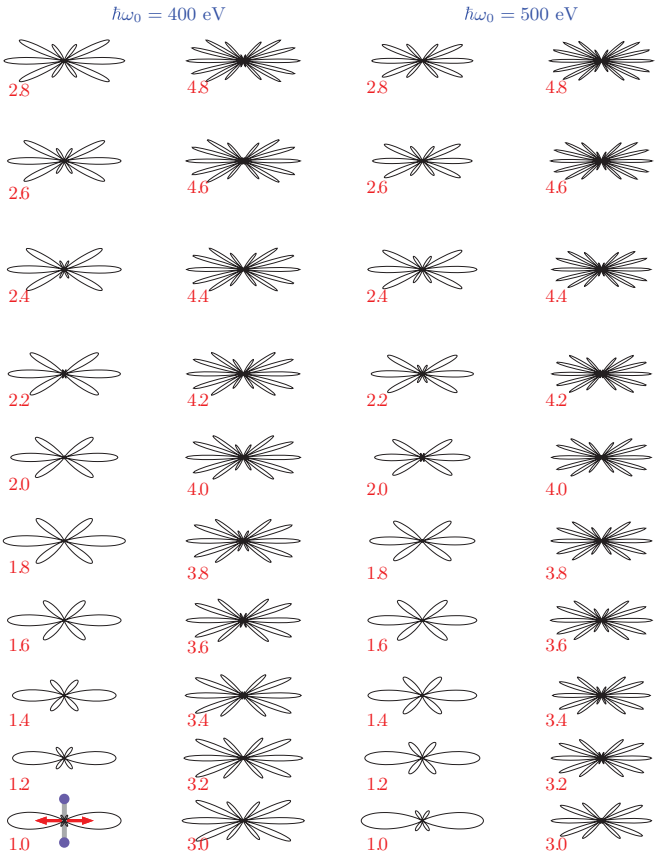

FIG. 6. (Color online) Same as Fig. 2, but for the perpendicular geometry.

axis. This intrinsic characteristic associated with the dipole transition also occurs in the plane-wave model, due to the term $(\boldsymbol{\epsilon}\cdot\boldsymbol{k})^2$.

We emphasize that the interference effect in the perpendicular geometry is different from that in the parallel case. According to the plane-wave model, the maxima in the angular distributions for the perpendicular geometry appear when the condition $\cos(\theta_{kR}) = 2n\pi/(kR)$ is fulfilled. Here n is an integer and θ_{kR} denotes the angle between $\boldsymbol{k}$ and the molecular axis. At the photon energy of 500 eV and $R = 4.8$ bohr, for example, the plane-wave model predicts five peaks in the angular distributions for $0^\circ \leqslant \theta_{kR} \leqslant 90^\circ$. Specifically, they are at $\theta_{kR} = 90.0^\circ, 75.6^\circ, 60.3^\circ, 42.0^\circ$, and 7.8°, respectively. This is in qualitative agreement with our numerical solutions (see Fig. 6), in particular, for the large angles. Our predictions are 90.0°, 77.5°, 64.6°, 49.6°, and 31.1°, respectively, for these five maxima. The plane-wave model is not accurate when the angular distributions are relatively small, which corresponds to small angles θ_{kR}.

Overall, the plane-wave model predicts the essential physics correctly in most cases, although the details are not the same as in our numerical results. Therefore, one might wonder how the angular distribution determined by Eq. (6) and $(\boldsymbol{\epsilon}\cdot\boldsymbol{k})^2\cos^2(\boldsymbol{k}\cdot\boldsymbol{R}/2)$ from the plane-wave model are related. In our present formalism [cf. Eq. (6)], the angular part of the momentum $\boldsymbol{k}$ is contained in the *spheroidal* harmonics functions $\mathcal{Y}_{\ell m}(\boldsymbol{k})$, which are further expanded in terms of spherical harmonics $Y_{\ell m}(\hat{\boldsymbol{k}})$ with the same parity (odd here) and magnetic quantum number m. In the molecular frame, where the direction of $\hat{\boldsymbol{k}}$ is measured with respect to the molecular axis, the odd-order $Y_{\ell 0}(\hat{\boldsymbol{k}})$ functions contain a factor $\cos\theta$ in the parallel geometry while the $Y_{\ell 1}(\hat{\boldsymbol{k}})$ functions contain $\sin\theta$ in the perpendicular geometry. This is independent of the magnitude of the momentum k. Consequently, the angle-differential cross section is proportional to $\cos^2\theta$ in the parallel case and to $\sin^2\theta$ in the perpendicular geometry. Both cases can be unified as $(\boldsymbol{\epsilon}\cdot\hat{\boldsymbol{k}})^2$. This result is independent of the relative angle between the $\boldsymbol{\epsilon}$ and $\boldsymbol{\zeta}$ axes, and it is also independent of the internuclear separation. Hence the partial angular dependence, $(\boldsymbol{\epsilon}\cdot\hat{\boldsymbol{k}})^2$, predicted in the plane-wave model is correct not only for atoms but also for molecules in single-photon ionization.

At this point, we can separate the contributions to the photoelectron DCS for diatomic molecules into two parts: the first one is the universal term $(\boldsymbol{\epsilon}\cdot\hat{\boldsymbol{k}})^2$ discussed above while the second part contains information about the multicenter nonspherical molecular effect. In other words, the difference between our Eq. (6) and the prediction of the plane-wave model lies in the second term, which contains the contributions from high-ℓ angular components.

Note that the plane-wave idea is used in both the quantum plane-wave model of Walter and Briggs [23] and the classical double-slit formalism. We might then ask whether or not they predict the same interference patterns. In both geometries, $kR\cos\theta_{kR} = 2n\pi$ and $R\sin\theta_n = n\lambda_e$ are indeed identical in predicting the angles of the maxima in the DCS and the bright fringes. However, the relative intensities are different. The intensity of the bright fringes in the double-slit setup is given by $\mathcal{I}(\theta_n) \propto \cos^2[\pi R\sin(\theta_n)/\lambda_e]$, which is the same as $\cos^2(\boldsymbol{k}\cdot\boldsymbol{R}/2)$. The universal term $(\boldsymbol{\epsilon}\cdot\hat{\boldsymbol{k}})^2$ in the quantum model, however, is missing in the double-slit counterpart.

This may indeed lead to noticeable modifications in the interference patterns. In particular, the difference in the predicted intensities is more visible in the parallel geometry because $(\boldsymbol{\epsilon}\cdot\hat{\boldsymbol{k}})^2 = \sin^2\theta_n$. Consequently, the primary fringe in the double-slit experiment ($\theta_0 = 0^\circ$) is missing in the quantum DCS for photoelectron emission from the H_2^+ ion in the parallel geometry. On the other hand, the primary peak always persists in the perpendicular geometry, since $(\boldsymbol{\epsilon}\cdot\hat{\boldsymbol{k}})^2 = \cos^2\theta_n$.

At this point, we realize that the DCS in the perpendicular geometry closely resembles the classical double-slit scenario, while it does not do so in the parallel case. From the discussion above, the term $(\boldsymbol{\epsilon}\cdot\hat{\boldsymbol{k}})^2$ is universal for single-photon ionization in both atomic and diatomic targets. It simply shows that the geometrical factor in the quantum dipole transition is determined by a selection rule. This is a pure quantum effect and therefore lacks a classical counterpart. Depending on where the nodes appear in the final continuum states, the primary fringe observed in the classical double-slit experiment may or may not survive in a quantum two-center target.

IV. PROBABILITY DENSITIES IN THE PARALLEL AND PERPENDICULAR GEOMETRIES

Figures 7 and 8 display the probability densities ($|\Psi(\boldsymbol{r},t)|^2$) in configuration space and the momentum distributions

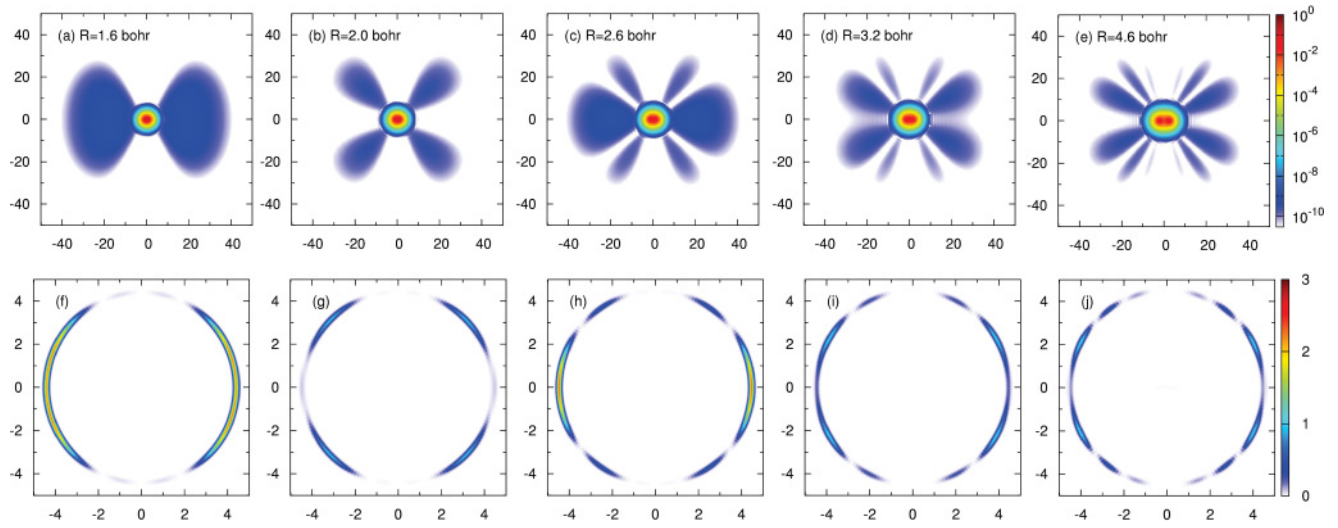

FIG. 7. (Color online) Probability densities (a)–(e) and momentum distributions (f)–(j) of the photoelectron from the H_2^+ ion at the end of the laser pulse for the parallel geometry. The laser pulse, with a sine-squared envelope function, contains 20 cycles. It has a central photon energy of 300 eV and a peak intensity of 10^{16} W/cm^2. The polarization axis of the laser is oriented horizontally. The momentum distributions ($dP_{\rm ion}/d\boldsymbol{k}$) are presented in units of 10^{-6} per momentum in a.u. The dimensions in the configuration space (top row) are given in units of bohr, while the momentum space (bottom row) is in a.u.

($dP_{\rm ion}/d\boldsymbol{k}$) at the end of the laser pulse, respectively, in the parallel and perpendicular geometries. Rich information on the ionization dynamics is already revealed after examining $|\Psi(\boldsymbol{r},t)|^2$ in configuration space. There is a one-to-one correspondence between the patterns seen in the configuration and momentum spaces for the preferable directions of emission modes. Although the time evolution of the wave packet $|\Psi(\boldsymbol{r},t)|^2$ does not directly reveal the dominant magnitude of the momentum of the photoelectron, it clearly shows both the preferable and forbidden emission directions. For some cases, particularly in the parallel geometry, the probability density for the electron being ionized along the polarization axis is completely negligible [cf. Fig. 7(b) at $R = 2.0$ bohr]. This corresponds to the confinement effect observed in the angle-resolved momentum distribution [cf. Fig. 7(g) at the same R].

Similar correspondences can also be established for the perpendicular geometry (cf. Fig. 8). At large values of R, well-resolved bouquet-shaped probability densities in the perpendicular geometry are directly related to the double-slit interference patterns observed in the momentum distributions.

In order to further visualize the time development of the angular distribution pattern, we have created QUICKTIME movies for selected cases (see Ref. [24]).

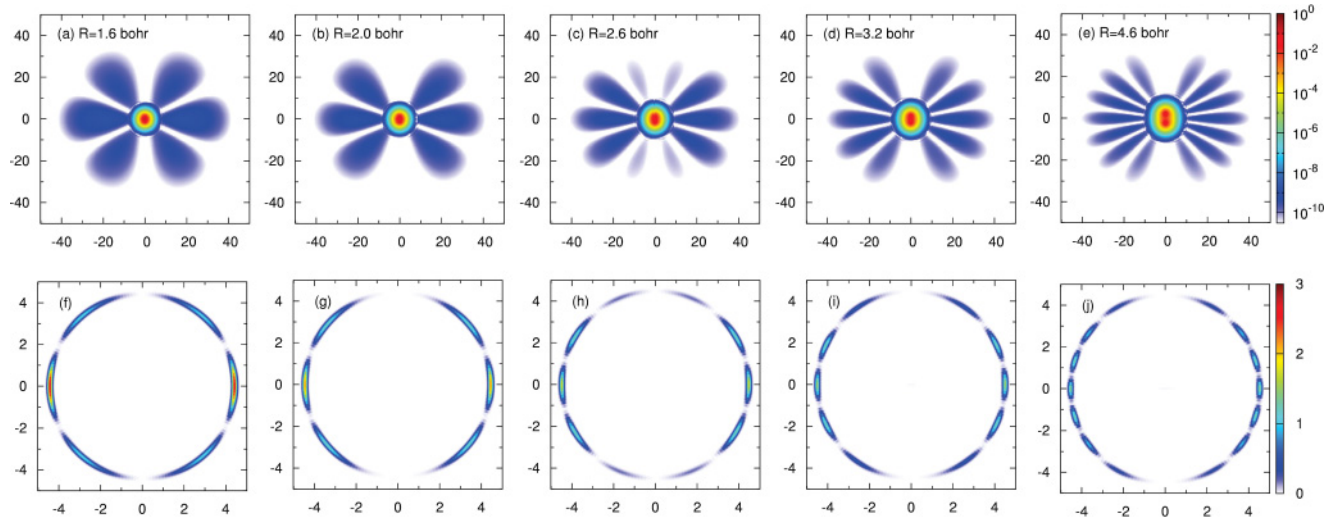

FIG. 8. (Color online) Same as Fig. 7, but for the perpendicular geometry. The molecular axis is oriented along the vertical direction, while the polarization axis of the laser pulse is along the horizontal direction.

V. SUMMARY AND OUTLOOK

We have investigated the photoionization of the homonuclear hydrogen molecular ion irradiated by an x-ray laser at high photon energies between 200 and 500 eV. We solved the TDSE in two-center prolate spheroidal coordinates in the fixed-nuclei approximation. The connection between the angular distributions of the photoelectron and the classical double-slit interference was discussed for both the parallel and perpendicular geometries. The similarities and differences between the predictions from our accurate *ab initio* calculations, a plane-wave model, and classical double-slit interference were analyzed.

Photoionization of heteronuclear molecular ions such as HeH^{2+} [25,26] may provide even more interesting perspectives to depict two-center interference patterns. Not only would we need to launch the HeH^{2+} ion from an initial state with a different symmetry ($1s\sigma$ does not support a bound state in this case), but the intensities of the electronic wave packets emitted from the two nuclei will differ as well. Therefore, the complete scenario comparing classical double-slit-like interference and photoionization in a general two-center molecular target can be established. Work in this direction is currently in progress in our group.

The present study is also an important stepping stone toward the investigation of much more challenging two-electron phenomena. Our long-term goal is to explore the essential differences in the electron diffraction pattern between two-electron waves and one-electron waves from H_2. This will enable us to better understand the role of correlation effects in the interference patterns between the two ionized two-electron wave packets. Recall that double ionization is forbidden without correlation between the two electrons in single-photon ionization [20].

ACKNOWLEDGMENTS

This work was supported by the United States National Science Foundation under Grant No. PHY-1068140 (X.G. and K.B.) and the XSEDE Allocation No. PHY-090031. Additional support from Drake University through a Troyer Research Fellowship (K.B.) is also gratefully acknowledged.

[1] H. D. Cohen and U. Fano, Phys. Rev. **150**, 30 (1966).
[2] I. G. Kaplan and A. P. Markin, Sov. Phys. Dokl. **14**, 36 (1969).
[3] C. Jönnson, Z. Phys. A **161**, 454 (1961).
[4] M. W. Noel and C. R. Stroud, Phys. Rev. Lett. **75**, 1252 (1995).
[5] L. Ph. H. Schmidt, T. Jahnke, A. Czasch, M. Schöffler, H. Schmidt-Böcking, and R. Dörner, Phys. Rev. Lett. **108**, 073202 (2012).
[6] *Many-Particle Quantum Dynamics in Atomic and Molecular Fragmentation*, edited by J. Ullrich and V. Shevelko (Springer-Verlag, Berlin, 2003).
[7] D. Akoury *et al*., Science **318**, 949 (2007).
[8] K. Kreidi *et al*., Phys. Rev. Lett. **100**, 133005 (2008).
[9] D. A. Horner, S. Miyabe, T. N. Rescigno, C. W. McCurdy, F. Morales, and F. Martin, Phys. Rev. Lett. **101**, 183002 (2008).
[10] S. E. Canton, E. Plésiat, J. D. Bozek, B. S. Rude, P. Decleva, and F. Martín, Proc. Natl. Acad. Sci. USA **108**, 7302 (2011).
[11] http://www-als.lbl.gov/.
[12] J. Fernández, F. L. Yip, T. N. Rescigno, C. W. McCurdy, and F. Martín, Phys. Rev. A **79**, 043409 (2009).
[13] J. Fernández, O. Fojón, A. Palacios, and F. Martín, Phys. Rev. Lett. **98**, 043005 (2007).
[14] K. J. Yuan, H. Z. Lu, and A. D. Bandrauk, Phys. Rev. A **80**, 061403 (2009).
[15] K. J. Yuan, H. Z. Lu, and A. D. Bandrauk, Phys. Rev. A **83**, 043418 (2011).
[16] S. X. Hu, L. A. Collins, and B. I. Schneider, Phys. Rev. A **80**, 023426 (2009).
[17] X. Guan, E. B. Secor, K. Bartschat, and B. I. Schneider, Phys. Rev. A **84**, 033420 (2011).
[18] M. Foster, J. Colgan, O. Al-Hagan, J. L. Peacher, D. H. Madison, and M. S. Pindzola, Phys. Rev. A **75**, 062707 (2007).
[19] J. Colgan, A. Huetz, T. J. Reddish, and M. S. Pindzola, J. Phys. B **41**, 085202 (2008).
[20] X. Guan, K. Bartschat, and B. I. Schneider, Phys. Rev. A **83**, 043403 (2011).
[21] X. Guan and K. Bartschat, Phys. Rev. Lett. **103**, 213201 (2009).
[22] A. S. Baltenkov, U. Becker, S. T. Manson, and A. Z. Msezane, J. Phys. B **45**, 035202 (2012).
[23] M. Walter and J. Briggs, J. Phys. B **32**, 2487 (1999).
[24] http://bartschat.drake.edu/H2+interference.html
[25] D. R. Bates and T. R. Carson, Proc. R. Soc. London, Ser. A **234**, 207 (1956).
[26] I. Ben-Itzhak, I. Gertner, O. Heber, and B. Rosner, Phys. Rev. Lett. **71**, 1347 (1993).